JAMES | Journal of Advances in Modeling Earth Systems

RESEARCH ARTICLE
10.1029/2023MS003968

ITCZ Response to Disabling Parameterized Convection in Global Fixed-SST GFDL-AM4 Aquaplanet Simulations at 50 and 6 km Resolutions

Joseph P. Clark[1], **Pu Lin**[1], **and Spencer A. Hill**[2]

[1]Program in Atmospheric and Oceanic Sciences, Princeton University, Princeton, NJ, USA, [2]Department of Earth and Atmospheric Sciences, City College of New York, New York, NY, USA

Key Points:

- Disabling parameterized convection changes the InterTropical Convergence Zone (ITCZ) precipitation minus evaporation maximum by +78% and −50% at 50 and 6 km resolutions
- Disabling parameterized convection at 6 km resolution deepens the Hadley circulation, increasing gross moist stability
- Disabling parameterized convection at 50 km resolution increases subtropical cloud radiative cooling, intensifying the Hadley circulation

Supporting Information:

Supporting Information may be found in the online version of this article.

Correspondence to:

J. P. Clark,
jc7377@princeton.edu

Citation:

Clark, J. P., Lin, P., & Hill, S. A. (2024). ITCZ response to disabling parameterized convection in global fixed−SST GFDL-AM4 aquaplanet simulations at 50 and 6 km resolutions. *Journal of Advances in Modeling Earth Systems*, *16*, e2023MS003968. https://doi.org/10.1029/2023MS003968

Received 14 AUG 2023
Accepted 27 MAY 2024

Author Contributions:

Conceptualization: Joseph P. Clark, Pu Lin, Spencer A. Hill
Formal analysis: Joseph P. Clark
Investigation: Joseph P. Clark, Pu Lin, Spencer A. Hill
Methodology: Joseph P. Clark, Pu Lin, Spencer A. Hill
Resources: Pu Lin, Spencer A. Hill
Supervision: Pu Lin, Spencer A. Hill
Visualization: Joseph P. Clark

Abstract As the community increases climate model horizontal resolutions and experiments with removing moist convective parameterizations entirely, it is imperative to understand how these advances affect the InterTropical Convergence Zone (ITCZ). We investigate how the ITCZ responds to deactivating parameterized convection at two resolutions, 50 and 6 km, in fixed sea surface temperature, aquaplanet simulations with the NOAA GFDL AM4 atmospheric model. Disabling parameterized convection at 50 km resolution narrows the ITCZ and increases its precipitation minus evaporation (P–E) maximum by ∼78%, whereas at 6 km resolution doing so widens the ITCZ and decreases its P–E maximum by ∼50%. Using the column-integrated moist static energy budget, we decompose these tropical P–E responses into contributions from changes in atmospheric energy input (AEI), gross moist stability, and gross moisture stratification. At 6 km, the ITCZ weakens due to increased gross moist stability. Disabling the convective parameterization at this finer resolution deepens the circulation, favoring more efficient poleward energy transport out of the deep tropics and reduced precipitation in the core of the ITCZ. Conversely, at 50 km the ITCZ strengthening is primarily driven by AEI, which in turn stems primarily from increased low cloud amount and thus longwave cloud radiative cooling in the Hadley cell subsiding branch. The Hadley circulation overturning intensifies to produce poleward energy fluxes that compensate the longwave cooling, yielding a stronger ITCZ. We further show that the low level diabatic heating profiles over the descending region are instrumental in understanding such diverse responses.

Plain Language Summary About one-third of Earth's precipitation falls within a narrow band near the equator, the InterTropical Convergence Zone (ITCZ). In this study, we investigate two modeling choices that affect the ITCZ: (a) the horizontal resolution of the model and (b) the convective parameterization, which controls how heat and water ascend within thunderstorms and clouds. We conduct four simulations using an idealized climate model setup that assumes the globe is wholly ocean with unchanging surface temperatures. One pair of simulations is conducted at 50 km resolution and the other pair of simulations is conducted at 6 km resolution. Both pairs of simulations compare the ITCZ with and without an active convective parameterization. The ITCZ precipitation maximum nearly doubles when deactivating the convective parameterization at 50 km resolution, however, at 6 km resolution, the ITCZ precipitation maximum halves. The reasons for these disparate ITCZ changes relate to how much, and how efficiently, energy is transported by the Hadley circulation. Whereas at 50 km, deactivating the convective parameterization promotes low clouds that cool the subtropics, accelerating the Hadley circulation and raising precipitation, at 6 km, deactivating the convective parameterization instead increases the efficiency with which energy is transported by the Hadley circulation, reducing precipitation.

1. Introduction

About one-third of Earth's precipitation occurs within the InterTropical Convergence Zone (ITCZ; Kang et al., 2018), a meridionally confined region of low-level mass flux convergence within the ascending branch of the zonal-mean Hadley circulation. Consequently, the ITCZ fundamentally shapes tropical climate, rendering the processes that control ITCZ variations an important topic. Despite a wide range of theories on ITCZ dynamics (Bischoff & Schneider, 2014, 2016; Broccoli et al., 2006; Byrne & Schneider, 2016a, 2016b; Hill, 2019; Kang et al., 2008, 2009; Marshall et al., 2014; Schneider et al., 2014), the ITCZ remains notoriously biased in global climate model (GCM) simulations (e.g., Lin, 2007; Tian & Dong, 2020). The likely ITCZ changes in the future

Writing – original draft: Joseph P. Clark
Writing – review & editing: Pu Lin, Spencer A. Hill

(e.g., Byrne et al., 2018; Byrne & Schneider, 2016b) present a pressing motivation to improve how models represent the ITCZ.

A major impediment is the ITCZ's pronounced sensitivity to configurational choices, often eluding physical explanations. Noted modeling choices that impact the ITCZ width, intensity and position include horizontal resolution (e.g., Benedict et al., 2017; Landu et al., 2014; Rios-Berrios et al., 2022), vertical resolution (e.g., Retsch et al., 2017), time step (e.g., Mishra et al., 2008), dynamical core solver (e.g., Landu et al., 2014) and various physical parameterizations (e.g., Chao & Chen, 2004; Frierson, 2007; Kang et al., 2008, 2009; Liu et al., 2010; Möbis & Stevens, 2012; Rios-Berrios et al., 2022; Song & Zhang, 2018; Voigt et al., 2014). In particular, switching convection schemes (e.g., Chao & Chen, 2004; Hess et al., 1993; Liu et al., 2010; Nolan et al., 2016; Song & Zhang, 2018), modifying parameters within a given convection scheme (e.g., Hess et al., 1993; Kang et al., 2009; Nolan et al., 2016), or disabling a convection scheme altogether (e.g., Frierson, 2007; Möbis & Stevens, 2012; Nolan et al., 2016) are each known to impact climatological precipitation within the ITCZ. These sensitivities represent much of the motivation for ongoing experiments with storm-resolving models (SRMs), increasing horizontal resolutions toward storm resolving scales (i.e., horizontal resolutions of a few kilometers; e.g., Stevens et al., 2019), where grid scale motions may begin to resolve deep convection (e.g., Pauluis & Garner, 2006; Weismann et al., 1997), though certainly not shallow convection (e.g., Bryan et al., 2003).

How the ITCZ responds to disabling parameterized convection has varied across prior studies, both at resolutions typical of current GCMs and at resolutions typical of SRMs. At GCM-like resolutions, disabling the convection scheme typically intensifies ITCZ precipitation (Frierson, 2007; Möbis & Stevens, 2012; Retsch et al., 2019). Nevertheless, 46 km aquachannel simulations of the Weather Research and Forecasting Model (WRF; Skamarock et al., 2008) exhibited responses to disabling the deep convection scheme that depended on the deep convective parameterization used in the model (with shallow convection enabled; Nolan et al., 2016; their Figure A1).

At SRM-like resolutions, different ITCZ responses have been documented (Nolan et al., 2016; Rios-Berrios et al., 2022). In an aquaplanet configuration of the Model for Prediction Across Scales-Atmosphere (MPAS-A; Skamarock et al., 2012), a simulation run at 3 km resolution with the deep convection scheme disabled intensifies the ITCZ precipitation maximum compared to runs at 15–30 km resolution with the scheme enabled (Rios-Berrios et al., 2022). But in an aquachannel configuration of WRF, a simulation run at 5 km resolution with the deep convection scheme disabled reduces the ITCZ precipitation maximum compared to runs at 46–139 km with the scheme enabled (Nolan et al., 2016). Notably it is unclear from either Nolan et al. (2016) and Rios-Berrios et al. (2022) how disabling *both* the shallow and deep convection schemes would impact the ITCZ, or what the response would be at a fixed SRM-like resolution.

Different physical mechanisms have been invoked to explain the ITCZ changes in the above studies. At GCM-like resolutions, Möbis and Stevens (2012) argue that the ITCZ response in ECHAM6 represents a coupled feedback wherein changes in convective heating modify surface winds, which in turn modify the boundary layer moist static energy (MSE) through changes in surface fluxes. The elevated boundary layer MSE then intensifies convection in the ITCZ. At SRM-like resolutions, Rios-Berrios et al. (2022) and Nolan et al. (2016) both relate the ITCZ response to changes in cold pools.

Other studies on the sensitivity of the ITCZ to various modeling choices more broadly emphasize feedbacks between clouds and the circulation (e.g., Dixit et al., 2018; Harrop & Hartmann, 2016; Popp & Silvers, 2017). For example, previous studies have shown that longwave cloud radiative effects act to narrow the ITCZ (Harrop & Hartmann, 2016; Popp & Silvers, 2017) and that high and low clouds can have different effects on the ITCZ width (Dixit et al., 2018). Given these findings and that the convection scheme affects clouds, a reasonable presumption is that clouds play a role in the ITCZ response to disabling convection. For example, Hohenegger et al. (2020) found that in 10–80 km runs of the ICON model with the convection scheme disabled, low cloud amounts increased with decreasing resolution, attributed to a deeper mixed layer and a stronger low-level inversion. These findings suggest that clouds likely play a role in the ITCZ response to disabling parameterized convection, but the exact mechanisms through which clouds contribute remain unestablished.

This landscape of conflicting results both within and across GCM versus SRM resolutions motivates this study, in which we disable the convection scheme at 50 km resolution and at 6 km resolution in a fixed-SST aquaplanet configuration, a clean 2 × 2 matrix of simulations meant to isolate the salient physical mechanisms at both

resolutions in one model. In Section 2, we discuss the model simulations and methods used. In Section 3, we present the results and our physical interpretations. We conclude in Section 4 and discuss broader implications.

2. Model Simulations and Methods

2.1. Simulations

We examine simulations from the NOAA Geophysical Fluid Dynamics Laboratory AM4 atmospheric GCM in its alternative "AM4-MG2" configuration, a well-tested configuration that will form the base of future AM models (Guo et al., 2021; Lin et al., 2023). The model employs the standard AM4 physics package (Zhao et al., 2018a; Zhao et al., 2018b), but with more sophisticated microphysics (Gettelman & Morrison, 2015) and a non-hydrostatic solver (Harris et al., 2020). The simulations are configured as an aquaplanet with fixed SSTs specified as the Q-control profile from Neale and Hoskins (2000) and perpetual equinox insolation including a diurnal cycle. Details of the model settings are documented in Lin et al. (2023).

Our primary focus centers on two nearly identical pairs of simulations at 50 km and at 6 km. In one pair, the model physics are unmodified, and in the other pair the convective parameterization is deactivated entirely, with no other retuning. This 2×2 matrix of simulations (50 km_on, 50 km_off; 6 km_on, 6 km_off) and the idealized boundary conditions enable us to pinpoint how disabling this model's convective parameterization affects the ITCZ and how that depends on resolution. In a fifth simulation, we isolate the relative influence of deep and shallow convection at 50 km resolution by disabling only the deep plume while keeping the shallow plume active (50 km_shallow; see below). Each of the five simulations span 1 year; we discard the first 3 months as spin-up and investigate time-averaged fields over the remaining 9 months which is sufficiently long for the zonal mean climatological precipitation to stabilize. All fields from both models are coarse-grained to a common $0.5° \times 0.5°$ grid using conservative remapping.

The convection scheme in AM4 includes two bulk plumes: one for shallow convection and one for deep convection (Zhao et al., 2018b). For both plumes, the representation of vertical velocity, the buoyancy sorting formulation, and the assumptions underlying the determination of the entrainment and detrainment rates follow directly from Bretherton et al. (2004), except with a different parameterization for the fractional lateral mixing rates (Zhao et al., 2018b). In addition, AM4 uses independent closures for the shallow and deep plumes. The closures for the cloud base mass flux are based on the cloud work function for the deep plume versus convective inhibition and boundary layer turbulent velocities for the shallow plume (Zhao et al., 2018b).

When both the shallow and deep plumes are deactivated in this study, all moist convection must result from grid-scale motions. In contrast, when both the shallow and deep plumes are turned on, precipitation is formed at the resolved scale, as well as from the shallow and deep convection schemes (Zhao et al., 2018b). Note also that when the convection scheme is turned on, the deep plume activates often at 50 km resolution but rarely at 6 km resolution: the respective fractions of precipitation over 10°S–10°N from grid-scale motion, the deep plume, and the shallow plume are 67%, 23%, and 10% at 50 km and 90%, 3%, and 7% at 6 km resolution. The difference in the relative contribution from the deep plume between the two resolutions motivates our additional run, 50 km_shallow (see above), to determine how much of the response can be attributed to disabling deep versus shallow convection. AM4 uses a prognostic cloud scheme based on Tiedtke (1993), and large-scale precipitation is determined by condensation resolved at the grid scale (Zhao et al., 2018b).

2.2. Methods

To investigate the mechanisms behind the precipitation changes caused by deactivating the convection scheme, we begin with the time-mean column-integrated MSE and moisture budgets,

$$\overline{\mathrm{AEI}} = \nabla \cdot \left\{\overline{hv}\right\} = \frac{1}{a \cos\phi} \frac{\partial \cos\phi \left\{\overline{hv}\right\}}{\partial \phi}, \tag{1}$$

$$\overline{P} - \overline{E} = -\nabla \cdot \{\overline{qv}\} = -\frac{1}{a \cos\phi} \frac{\partial \cos\phi \{\overline{qv}\}}{\partial \phi}, \tag{2}$$

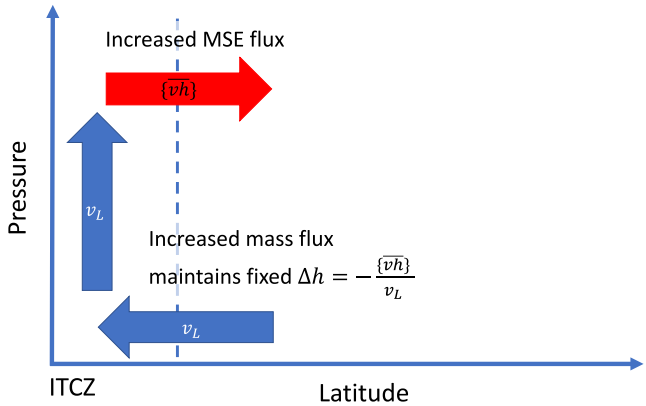

Figure 1. An idealized schematic illustrating how moist static energy fluxes must coincide with low level mass flux changes for fixed total gross moist stability.

where overbars denote a zonal and time mean, $\{\cdot\} \equiv \frac{1}{g}\int_0^{p_s} \cdot dp$ denotes a vertical integral from the surface pressure p_s to the top of the atmosphere, AEI denotes the AEI, v denotes meridional wind, h denotes MSE, and q denotes specific humidity. Note that the change in $\overline{P}-\overline{E}$ among these simulations is owed nearly entirely to changes in precipitation, $\overline{P}$, rather than from changes in evaporation, $\overline{E}$ (not shown). MSE is defined as the sum of sensible, latent and potential energy, $h = c_pT + L_vq + gz$, where c_p is the specific heat capacity of dry air at constant pressure, T is temperature, L_v is the latent heat of vapourization, g is gravity and z is the geopotential height. The atmospheric energy input, *AEI*, represents the energy taken up by the atmosphere, calculated as the difference between the energy flux at the top of the atmosphere and the surface via longwave and shortwave radiation as well as the surface sensible and latent heat fluxes.

Defining total gross moisture stratification $\Delta q \equiv \frac{\{\overline{qv}\}}{v_L}$ and total gross moist stability $\Delta h \equiv -\frac{\{\overline{hv}\}}{v_L}$, where $v_L \equiv \frac{1}{g}\int_{p_{max}}^{p_s} \overline{v}dp$ measures the mass fluxed by the zonal mean overturning circulation (The meridional wind was corrected by removing the vertically averaged zonal mean meridional wind to ensure no climatological poleward mass flux (see for example, Hill et al., 2015)), we combine Equations 1 and 2 following Kang et al. (2009),

$$\overline{P}-\overline{E} = \nabla\cdot\left(\frac{\Delta q}{\Delta h}\{\overline{hv}\}\right) = \nabla\cdot\left\{\frac{\Delta q}{\Delta h}\left[\frac{1}{\cos(\phi)}\int_{-\frac{\pi}{2}}^{\phi} a\cos(\phi)\,\overline{\mathrm{AEI}}d\phi\right]\right\}, \quad (3)$$

where ϕ denotes latitude and p_{max} represents the pressure level at which the zonal mean mass stream function maximizes; this corresponds to p_{max} = 811 hPa for all simulations except 50 km_off where p_{max} = 848 hPa.

For the conceptual basis of Equation 3, consider that an increase in low-level equatorward mass flux generally drives an increased moisture flux within the ITCZ, increasing P–E. Because Δh represents the ratio of poleward energy flux to low-level equatorward mass flux, for fixed Δh in Equation 3, any increase in poleward energy flux must be matched by an increase in low-level equatorward mass flux. This results in increased P–E within the ITCZ as illustrated schematically in Figure 1. On the other hand, if the meridional energy flux is maintained at a fixed value while the and gross moist stability (GMS) increases, this would imply a weaker low-level equatorward mass flux and thereby a reduced P–E within the ITCZ.

Although Equation 3 ultimately reduces to Equation 2, Equation 3 is useful because $\{\overline{hv}\}$, Δq, and Δh each have physically meaningful interpretations. Changes in the total meridional energy flux (We compute $\{\overline{hv}\}$ and $\{\overline{qv}\}$ by latitudinally integrating the left-hand sides of Equations 1 and 2. The global mean $\overline{AEI}$ and $\overline{P}-\overline{E}$ is subtracted before computing the integrals to ensure no residual at the pole. For both moisture and energy, eddies are computed as the residual between the total poleward transports and the mean meridional circulation (MMC) transport) $\{\overline{hv}\}$ can be related to changes in radiative and surface fluxes through Equation 1 while the quantities Δq and Δh respectively measure how efficiently moisture and energy are transported for a given Hadley cell strength (e.g., low level mass flux, v_L). The parameter Δq is the total gross moisture stratification (Kang et al., 2009), with "total" signifying that it includes the eddy contributions to the moisture flux in addition to that of the MMC. Similarly, the total gross moist stability Δh represents the total (MMC plus eddy) energy flux per unit mass flux in the lower troposphere (e.g., Kang et al., 2009). Following convention, we refer to the corresponding quantities that do not include the eddy contributions as simply the gross moisture stratification GMS respectively. Note also that although we use the definitions from Kang et al. (2009), these concepts were

originally defined to have a distinct meaning applied to energy, moisture, and mass flux divergences rather than meridional fluxes (e.g., Neelin & Held, 1987; Neelin & Yu, 1994; see review by Raymond et al., 2009).

Denoting δ as the P–E difference between the models with convection off versus on [$\delta \equiv (P-E)_{off} - (P-E)_{on}$] we can write the following expression:

$$\delta \approx \delta_{\mathrm{AEI}} + \delta_{\Delta h} + \delta_{\Delta q}, \tag{4}$$

where δ_{AEI}, $\delta_{\Delta h}$ and $\delta_{\Delta q}$ respectively denote the partial changes in P–E due to changes in AEI, Δh and Δq. We diagnose δ_{AEI}, $\delta_{\Delta h}$ and $\delta_{\Delta q}$ by independently perturbing AEI, Δh and Δq while holding the other two variables fixed. For example, δ_{AEI} is computed, with analogy to the two-sided partial radiative perturbation method (e.g., Colman & McAvaney, 1997), by perturbing AEI while fixing Δh and Δq to their values in the models with convection on, and again while fixing Δh and Δq to their values in the models with convection off. The average of these two perturbations gives our estimate of δ_{AEI},

$$\delta_{AEI} = \frac{1}{2}\left[g\left(\mathrm{AEI}_{off}, \Delta h_{on}, \Delta q_{on}\right) - g\left(\mathrm{AEI}_{on}, \Delta h_{on}, \Delta q_{on}\right)\right]$$

$$+\frac{1}{2}\left[g\left(\mathrm{AEI}_{off}, \Delta h_{off}, \Delta q_{off}\right) - g\left(\mathrm{AEI}_{on}, \Delta h_{off}, \Delta q_{off}\right)\right], \tag{5}$$

where g is a function defined by Equation 3. The partial changes due to Δh and Δq, $\delta_{\Delta h}$ and $\delta_{\Delta q}$, are defined analogously, where variables subscripted with "on" are taken from the model with the convection scheme on and variables subscripted with "off" from the model with the convection scheme off. The decomposition Equation 4 is done for 50 km_off minus 50 km_on and again for 6 km_off minus 6 km_on. For consistency and definiteness, we will refer to changes at a given resolution exclusively in terms of what happens when the convection scheme is disabled, that is, the "off" simulation minus the "on" simulation.

Before computing the terms in Equation 3, all fields are symmetrized about the equator given that an aquaplanet with fixed SST in perpetual equinox should not have any hemispheric differences over a long enough time average. Qualitatively, the results are not sensitive to the symmetrization, but symmetrization suppresses small interhemispheric differences that otherwise generate sharp and abrupt changes near the equator (see for example, Popp & Silvers, 2017).

3. Results

3.1. P–E Changes

Figures 2a and 2b show the climatological zonal mean P–E for each simulation. At 6 km resolution (Figure 2a), when the convection scheme is turned off, the P–E maximum approximately halves (from ∼17 to ∼8 mm/day) and the ITCZ widens. At 50 km resolution (Figure 2b), when the convection scheme is turned off, the P–E maximum nearly doubles (from ∼15 to ∼27 mm/day) and the ITCZ narrows. With the convection scheme activated, P–E differs only modestly between the two resolutions, suggesting approximate convergence in resolution (blue lines in Figures 2a and 2b). But with convection scheme deactivated, the resolution dependence is stark (red lines in Figures 2a and 2b).

Figures 2c and 2d show the P–E change δ decomposed into δ_{AEI}, $\delta_{\Delta h}$ and $\delta_{\Delta q}$. This decomposition Equation 4 holds to very good approximation (compare dashed-crossed black lines to solid black lines). At 50 km resolution, δ_{AEI} is about +8 mm/day over the equator, accounting for most of the change in P–E equatorward of 3° (Figure 2d). Between 3 and 5°, δ_{AEI} has a secondary contribution, behind $\delta_{\Delta h}$ which peaks in amplitude near −5 mm/day near 3° (Figure 2d). In contrast, at 6 km resolution $\delta_{\Delta h}$ predominates throughout the tropics (Figure 2c). Because $\delta_{\Delta q}$ is small at both resolutions, it will not be discussed further.

3.2. Total Gross Moist Stability at 6 km

To understand $\delta_{\Delta h}$, Figures 3a and 3b show Δh and Δh^{-1} for each model. Changes in Δh result in P–E changes that can be appreciated by considering Δh^{-1} (cf. Figures 3a and 3b), as Δh appears in the denominator of Equation 3. This can be seen in Figure 3b where we show that disabling parameterized convection at 6 km reduces

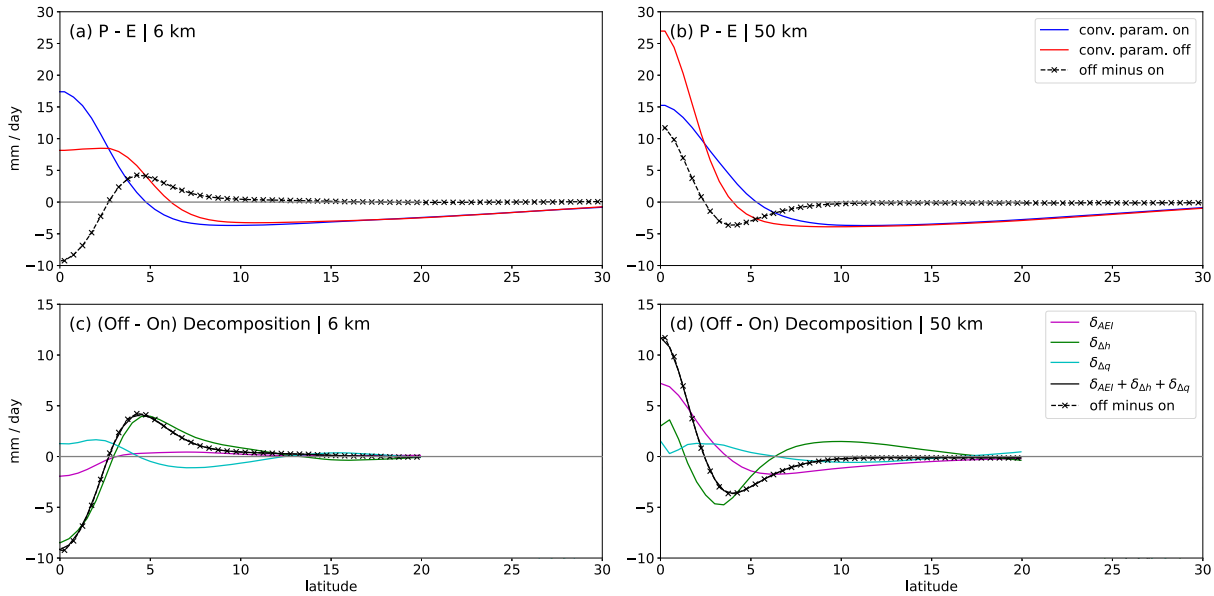

Figure 2. The climatological zonal mean precipitation minus evaporation from AM4-MG2 simulations with convection on (blue) and convection off (red) at 6 km resolution (left) and 50 km resolution (right). In the bottom row, the off minus on difference between precipitation minus evaporation is decomposed into contributions from atmospheric energy input (magenta), total gross moist stability (indigo) and total gross moisture stratification (cyan). See methods for details. The solid black lines in panels (c and d) show the sum of the magenta, green and cyan lines. In panels (c–d) lines are not plotted poleward 20° where the meridional wind approaches zero.

Δh^{-1} by about 0.2 kg/kJ–a change of about −50% at the equator. For fixed MSE transport, this reduction of Δh^{-1} reduces equatorward mass flux in the lower troposphere, decreasing P–E within the ITCZ, as captured by $\delta_{\Delta h}$ in Figure 2c (Something to keep in mind is that Δh^{-1} appears also within a gradient operator, and so $\delta_{\Delta h}$ has a contribution from changes in the Δh^{-1} gradient $[\Delta q\{\overline{hv}\}\nabla\cdot(\Delta h^{-1})]$ and amplitude $[\Delta h^{-1}\nabla\cdot(\Delta q\{\overline{hv}\})]$).

Because Δh represents the efficiency of MSE export accomplished by MSE transports from both eddies and the MMC (see Section 2), in Figure 4a we show Δh alongside its MMC and eddy components. We interpret the eddy component to Δh (i.e., the eddy GMS) as quantifying the impact of eddy MSE export on (P–E)—larger values indicating greater eddy MSE export and favoring reduced (P–E). Whereas the eddy GMS climatologically increases with latitude for both 6 km_off and 6 km_on (dotted lines), the MMC GMS (Δ_{MMC}, hereafter) first decreases modestly with latitude until about 5° before increasing with latitude thereafter (Figure 4a). In Figure 4b, we can see that the Δ_{MMC} response to disabling parameterized convection dominates over that of the eddy GMS.

Given that the Δ_{MMC} change dominates, we next split the Δ_{MMC} change into contributions independently attributable to circulation and MSE changes (Figure 5a). Using a two-sided difference method similar to Equation 5 we define the thermodynamic contribution to Δ_{MMC} as $\frac{1}{2}[g(v_{off}, h_{off}) - g(v_{off}, h_{on})] + \frac{1}{2}[g(v_{on}, h_{off}) - g(v_{on}, h_{on})]$, where $g = \frac{\{\overline{vh}\}}{v_L}$. The dynamic part is defined similarly. Although both MSE and circulation changes contribute to Δ_{MMC} changes (Figure 5a), the dynamic component is more important at all latitudes in the deep tropics, which implies a change in the circulation structure. This result can be conceptualized straightforwardly using a three-layer model we now introduce.

Averaging over the upper troposphere (above 400 hPa), mid troposphere (p_{max} to 400 hPa) and lower troposphere (below p_{max}) we approximate Δ_{MMC} as,

$$\Delta_{MMC} \approx -\frac{h_L v_L + h_M v_M + h_U v_U}{v_L}, \tag{6}$$

where h_L, h_M and h_U represent the MSE averaged over the lower, middle and upper troposphere, respectively, while v_M and v_U represent the poleward mass flux through the middle and upper troposphere, respectively. (Recall that v_L represents the mass flux in the lower troposphere as defined earlier). Three layers are chosen in Equation 6 to capture both the structure of the MMC and the C-shape typical of the MSE vertical profile (Figure S1 in

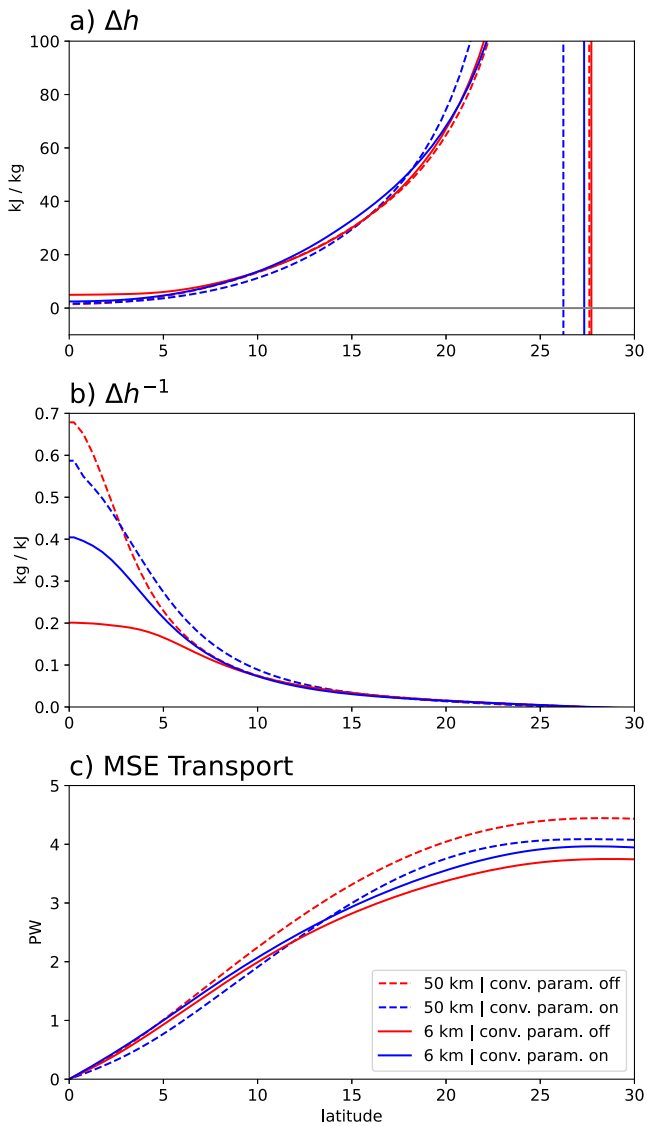

Figure 3. The (a) total gross moist stability, (b) inverse total gross moist stability and (c) moist static energy transport from AM4-MG2 simulations at 6 km resolution (solid lines) and 50 km resolution (dashed line) with convection on (blue lines) and convection off (red lines).

Supporting Information S1). Simplifying further by invoking mass conservation, $v_L = -(v_M + v_U)$, the following expression is derived,

$$\Delta_{MMC} \approx (h_U - h_L) + \frac{v_M}{v_L}(h_U - h_M), \tag{7}$$

which conveniently contains two terms with intuitive interpretations.

The first term on the right-hand side of Equation 7 also emerges in conventional two-layer representations of the tropical troposphere (e.g., Held, 2001). In this two-layer representation, a positive value for $(h_U - h_L)$ favors more efficient MSE export and a positive Δ_{MMC}. Further simplification arises by noting that, at all latitudes in the tropics, the tropical upper tropospheric temperature is set by the boundary layer MSE within the ITCZ. Specifically, assuming the vertical temperature profile over the equator is approximately moist adiabatic, we have $h_U(\phi = 0) = h_L(\phi = 0)$. Then, assuming weak temperature gradients in the tropical upper troposphere, $h_U = h_L(\phi = 0)$ at all latitudes in the tropics. Therefore, $h_U - h_L \approx h_L(\phi = 0) - h_L(\phi)$ (Held, 2001).

The second term in Equation 7 emerges by including a mid-tropospheric layer to capture the effect of changes in the vertical structure of the MMC. As indicated by Equation 6, the dynamic contribution to Δ_{MMC} is determined by $-\frac{v_M}{v_L}$, that is, the fraction of mass transported through the mid-troposphere by the shallower branch of the overturning circulation. Noting that $h_U > h_M$ due to the typical C-shape of the MSE profile (Figure S1 in Supporting Information S1), Equation 7 indicates that Δ_{MMC} decreases with increasing mid-level mass flux, $-\frac{v_M}{v_L}$. This is consistent with a shallower MMC being less efficient at fluxing MSE poleward. The second term on the right-hand side of Equation 7 can be further simplified by using an averaged value of 13.8 kJ/kg to represent $h_U - h_M$ (Figure S1 in Supporting Information S1; A similar value can be obtained if one assumes an the vertical profile that follows the moist adiabatic lapse rate from a surface temperature of 298 K, a scale height of 7 km and a constant relative humidity of 60% throughout the troposphere).

With this simple three-layer model, we find that the dynamic contribution to the Δ_{MMC} change is largely explained by changes in $\frac{v_M}{v_L} \cdot (13.8 kJ/kg)$ (Figure 5a; dotted cyan line). The thermodynamic term slightly offsets the dynamic term, which reflects a reduction in the low level MSE gradient due to the ITCZ drying at a greater rate than poleward latitudes in the tropics (presumably from reduced moisture flux). The Held (2001) scaling approximates the thermodynamic term reasonably well (Figure 5a; dotted magenta line).

Vertical profiles of the zonal mean meridional wind at the native vertical resolution elucidate where the relevant circulation changes are occurring (Figure 6a). Within 0–2°, 6 km_off is characterized by a top-heavy MMC (Figure 6a), with more poleward mass flux above 300 hPa and less poleward mass flux between 800 and 600 hPa, especially near 750 hPa, compared to 6 km_on. Though less pronounced, a similar conclusion can be made for the 6–10° latitude band. Thus, disabling parameterized convection at 6 km promotes a top-heavy the MMC, which increases Δ_{MMC} and reduces P–E within the ITCZ.

3.3. Atmospheric Energy Input at 6 km Resolution

Although nearly the entire change in P–E at 6 km resolution is due to changes in Δh (Figure 2c), for completeness and for comparison with the 50 km results, we briefly discuss why the AEI component is small at 6 km resolution. Figure 3c shows the poleward MSE transport for each of the four AM4 simulations, where considerable spread is evident. However, δ_{AEI} remains small at 6 km resolution (Figure 2c). This is because, as shown in Figure S2 in

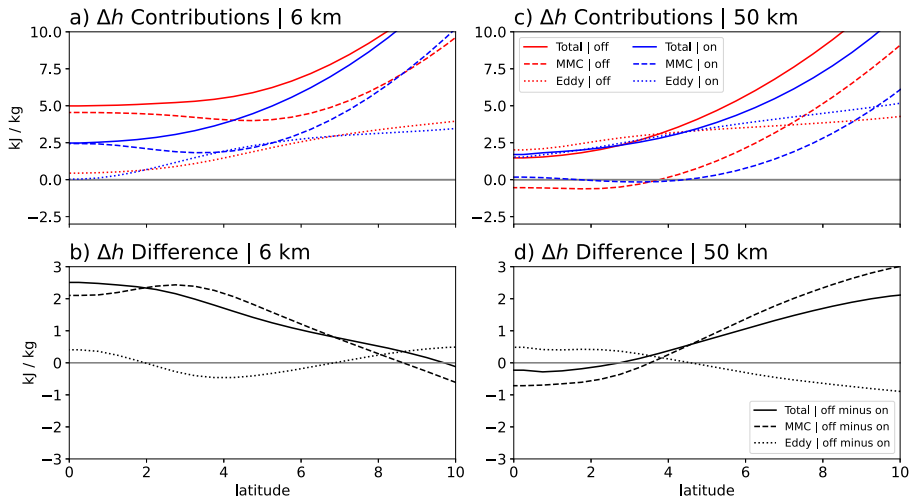

Figure 4. The total gross moist stability (solid), mean meridional circulation gross moist stability (dashed) and eddy gross moist stability (dotted) from AM4-MG2 simulations with convection off (red lines) and convection on (blues lines) at 6 km (left) and 50 km (right) resolutions. Panels (b, d) show the off minus on difference.

Supporting Information S1, changes in the longwave, shortwave and surface heat fluxes mostly cancel in the tropics, leading to near zero change in poleward MSE transport at latitudes in the vicinity of the ITCZ. However, that Δh^{-1} is much smaller at 6 km resolution is also an important consideration for understanding changes in δ_{AEI} because the quantity Δh^{-1} can be thought of as a measure for how much the low-level equatorward mass flux will change for a given change in poleward MSE transport. Because Δh^{-1} is climatologically reduced in the 6 km simulations relative to that in the 50 km simulations (Figure 3b), equatorward mass fluxes are less sensitive to MSE transport perturbations at 6 km resolution.

3.4. Atmospheric Energy Input at 50 km Resolution

In contrast with the 6 km results, when the convection scheme is disabled at 50 km, poleward MSE transport increases at all latitudes in the tropics, including at latitudes in the vicinity of the ITCZ (Figure 3c). For fixed Δh, this increase in poleward MSE transport will be accompanied by an increase in P–E within the ITCZ (see Figure 1), consistent with δ_{AEI} being positive within the ITCZ (Figure 2d).

Because any change in MSE transport must be associated with a change in AEI (see Equation 1), in Figure 7a we show the climatological AEI in 50 km_on and 50 km_off as a function of latitude. Whether parameterized convection is enabled or disabled, the climatological AEI is characterized by local maxima at about 5–10° (Figure 7a). However, when parameterized convection is disabled, AEI increases by about 12 W/m^2 over the

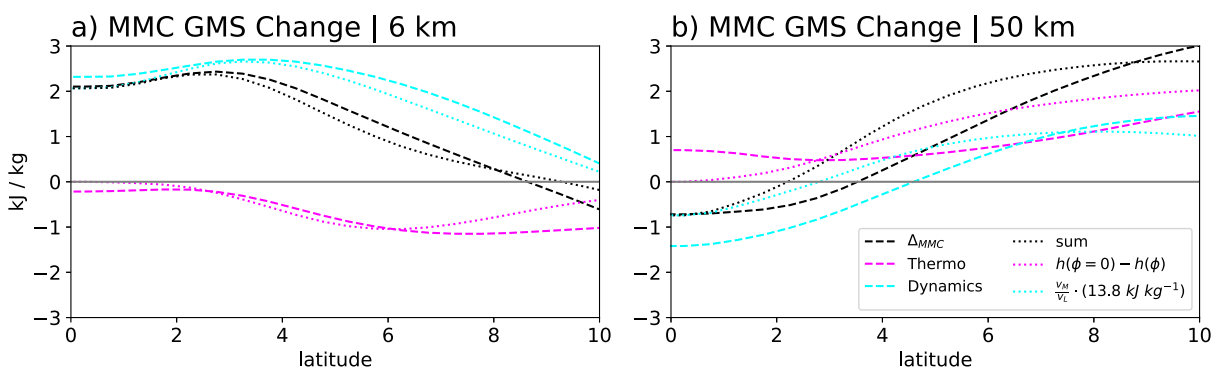

Figure 5. Decomposition of the change in the overturning circulation gross moist stability at (a) 6 km resolution and (b) 50 km resolution from AM4-MG2 simulations. The gross moist stability difference (black dashed) is decomposed into thermodynamic (MSE-driven; magenta) and dynamic (wind-driven; cyan) components. The dotted lines show a decomposition resulting from a simpler three-layer model (Equation 6).

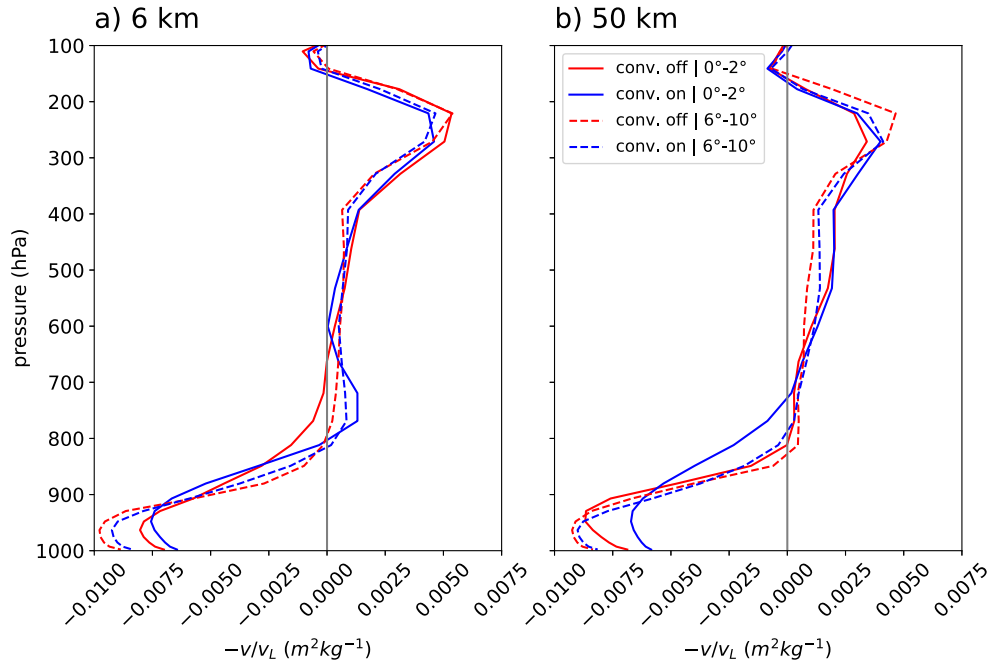

Figure 6. Vertical profiles of meridional wind averaged poleward over 6° through 10° (dashed lines) and equatorward of 2° in AM4-MG2 simulations at (a) 6 km and (b) 50 km resolution. The red lines show the runs with convection scheme disabled and the blue lines that with the convection scheme enabled.

equator (Figures 7a and 7b) (The local minimum over the equator is due primarily to weaker latent heat fluxes over the equator than in the subtropics; not shown).

We further decompose AEI changes into changes in shortwave radiation, longwave radiation, and surface sensible and latent heat fluxes. Shortwave radiation, surface sensible and latent heat fluxes contribute a positive AEI change, whereas longwave radiation contributes negatively, particularly over the subtropics (Figure 7b). The latitudinal variation in the AEI difference is mainly due to longwave radiation, specifically the cloud longwave radiative effects (dotted blue lines in Figure 7).

To determine which of these four components plays the most important role in the P–E response to disabling parameterized convection, we compute an implied change in low-level mass transport individually associated with each of these components as follows. First, we individually perturb the shortwave, longwave and surface flux components in the AEI budget Equation 1 and solve for the change in MSE transport due to this perturbation. Prior to computing the change in MSE transport due to the AEI perturbation, we avoid the unphysical result of non-zero global mean AEI by removing the global mean AEI imbalance introduced by the AEI perturbation. After this, these MSE transport perturbations are multiplied by Δh^{-1} averaged between 50 km_off and 50 km_on. The result is displayed in Figure 7c.

While each term in the AEI budget changes the low-level mass transport to a certain extent, the longwave component to the AEI change dominates, suggesting that the longwave component importantly contributes to δ_{AEI}. To confirm this, we compute the implied moisture fluxes obtained by multiplying the curves in Figure 7c by the total gross moisture stratification averaged between 50 km_on and 50 km_off. From the moisture fluxes, we determine the P–E response due independently to the longwave, shortwave and surface flux components in the AEI budget (Figure 7d). Consistent with the longwave component driving heightened mass flux convergence in the core of the ITCZ (Figure 7c), the longwave component to the AEI budget also drives a large increase in P–E in the core of the ITCZ (Figure 7d).

Figures 8a–8c elucidate why the longwave radiation change is pronounced; when the convection scheme is disabled, the climatological low-level cloud fraction increases to values in excess of 70% (Figures 8a–8c) consistent with a stronger low-level inversion (Figure 9a). These low cloud changes strongly collocate with changes in longwave radiative cooling (Figures 8d–8f), showing that disabling parameterized convection drives

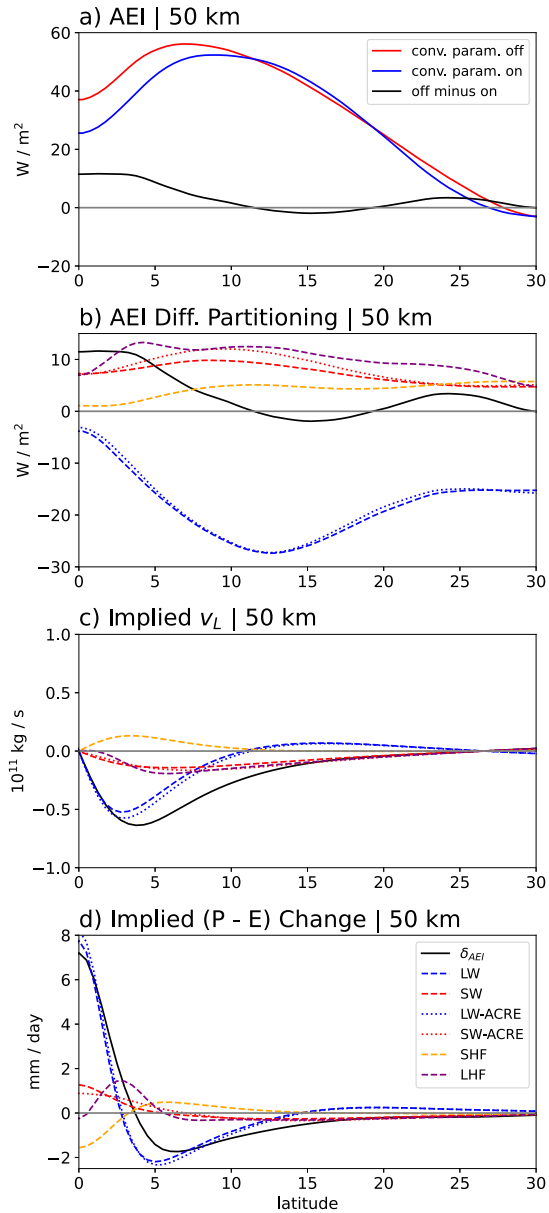

Figure 7. The (a) atmospheric energy input (AEI) from AM4-MG2 simulations at 50 km resolution with convection on (blue) and convection off (red). The off minus on difference (black line) is partitioned (b) into longwave radiation, shortwave radiation, their cloud radiative effects (denoted "ACRE"), latent and sensible heat fluxes. Panels (c) and (d) respectively show the implied low-level mass flux changes and precipitation changes calculated from the change in AEI (see Section 3.3).

an increase in low clouds that subsequently cool the subtropics through longwave radiation. For fixed Δh the poleward MSE fluxes are needed to balance the longwave cloud radiative cooling in the subtropics, resulting in a stronger MMC and more precipitation in the ITCZ.

Interestingly, Figure S3 in Supporting Information S1 demonstrates that the low cloud response in Figure 8 results from disabling the shallow plume rather than the deep plume. When only the deep convective parameterization is disabled (50 km_shallow), there are no significant changes in low cloud fraction (Figure S3 in Supporting Information S1). The low cloud changes in Figure 8 are therefore likely attributable to reduced ventilation of the boundary layer, a key function carried out by shallow convection. Evidence for this can be seen in Figure 9b, which shows a stark reduction of specific humidity between the 850 hPa and 700 hPa levels when the convection scheme is disabled. Increased low clouds are commonly observed when disabling the shallow convection parameterization in GCMs (e.g., McCaa & Bretherton, 2004; von Salzen et al., 2005; de Szoeke et al., 2006).

One may ask why the low cloud change in our study affects only the longwave rather than the shortwave component to AEI. Ultimately, this is because the atmosphere is mostly transparent to shortwave radiation. As Figure S4 in Supporting Information S1 illustrates, low clouds decrease downwelling shortwave radiation at the surface by nearly the same amount that they increase upwelling shortwave radiation at the top of the atmosphere. This results in a small change in the atmospheric uptake of shortwave radiation. In contrast, while the low clouds do not significantly impact the top of atmosphere upwelling longwave radiation because the low cloud temperature is nearly equal to the surface temperature, they do impact the surface longwave radiation through increasing the optical depth of the atmosphere (~25 W/m^2; Figure 7b). Thus, significant changes in downwelling longwave radiation at the surface (Figure S4 in Supporting Information S1) translate into large AEI changes. Such AEI changes must be accompanied by global mean precipitation changes (e.g., Watanabe et al., 2018). Interestingly, Hohenegger et al. (2020) report similar surface and top of atmosphere energy budget changes in their explicit convection simulations at 10–80 km resolution, due in part to changes in low cloud amounts.

3.5. Total Gross Moist Stability at 50 km

As with the 6 km case, to understand the Δh change at 50 km, in Figure 4c we plot Δ_{MMC} and the eddy GMS (Figures 4c and 4d). Both the eddy GMS and Δ_{MMC} increase with latitude throughout the tropics (Figure 4c). Interestingly, Δ_{MMC} is also negative, albeit slightly, in the deep tropics for the 50 km_off simulation (Figure 4c). In Figure 4d, we show that the Δh change is due mostly to the MMC. We therefore once again split the Δ_{MMC} change into thermodynamic and dynamic components and redeploy the approximation Equation 7 as a conceptual aid.

When redeployed at 50 km, Equation 7 is not as accurate as at 6 km (cf. Figures 5a and 5b), which we suspect is caused by two factors; (a) the streamfunction maxima occur at different levels between 50 km_on and 50 km_off and (b) disabling the shallow plume introduces a change to $(h_U - h_M)$ that is neglected by assuming $(h_U - h_M) \approx 13.8\mathrm{kJkg}^{-1}$. Nonetheless, the general shapes of the thermodynamic and dynamic responses are captured well enough for our conceptual purposes (Figure 5b). Comparing the approximate dynamic term, $\frac{v_M}{v_L} \cdot \left(13.8\ kJkg^{-1}\right)$ with the true dynamic term, we find agreement on the broad features: both terms are negative within the ITCZ and increase to positive values with increasing latitude. That the shape of $\frac{v_M}{v_L} \cdot \left(13.8 kJkg^{-1}\right)$ approximates dynamic contribution to the Δ_{MMC} change (Figure 5b) implies that within the ITCZ, where the

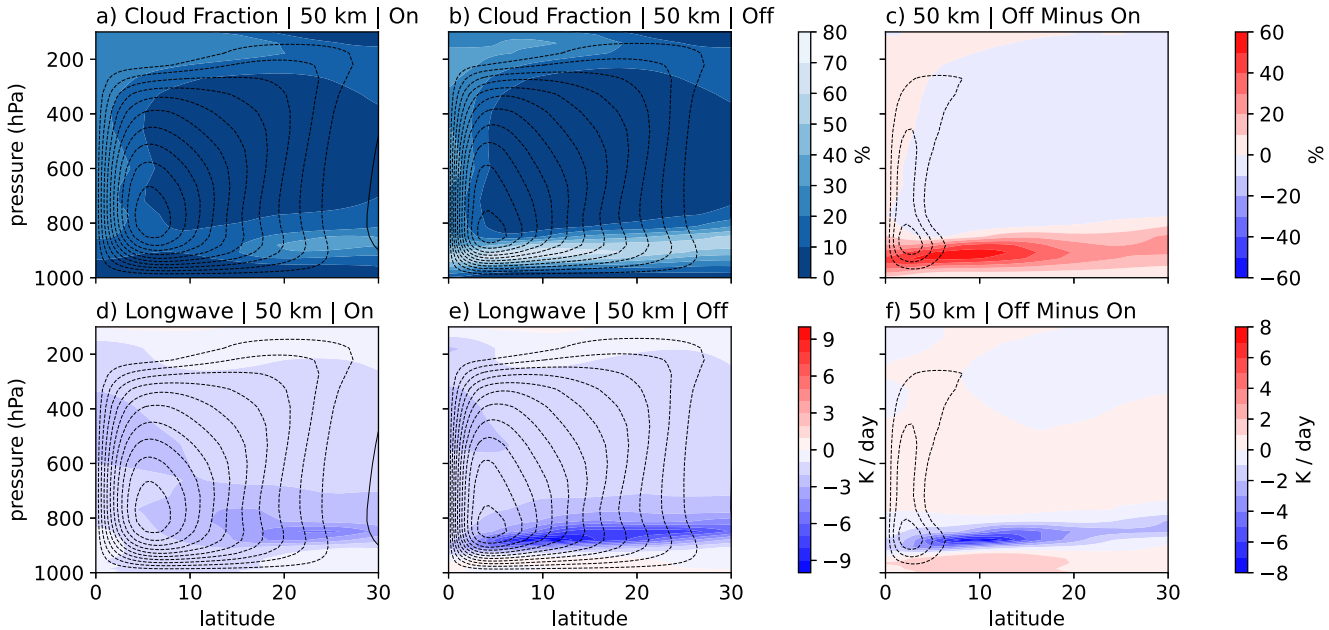

Figure 8. The climatological zonal mean (a, b) cloud fraction and (d, e) longwave radiative heating hemispherically averaged from AM4-MG2 simulations at 50 km resolution with convection on (left) and convection off (middle). The rightmost column shows the off minus on difference. The black contours show the Eulerian mass stream function where the contour interval is 2.0×10^{10} kg/s and the zero contour is omitted.

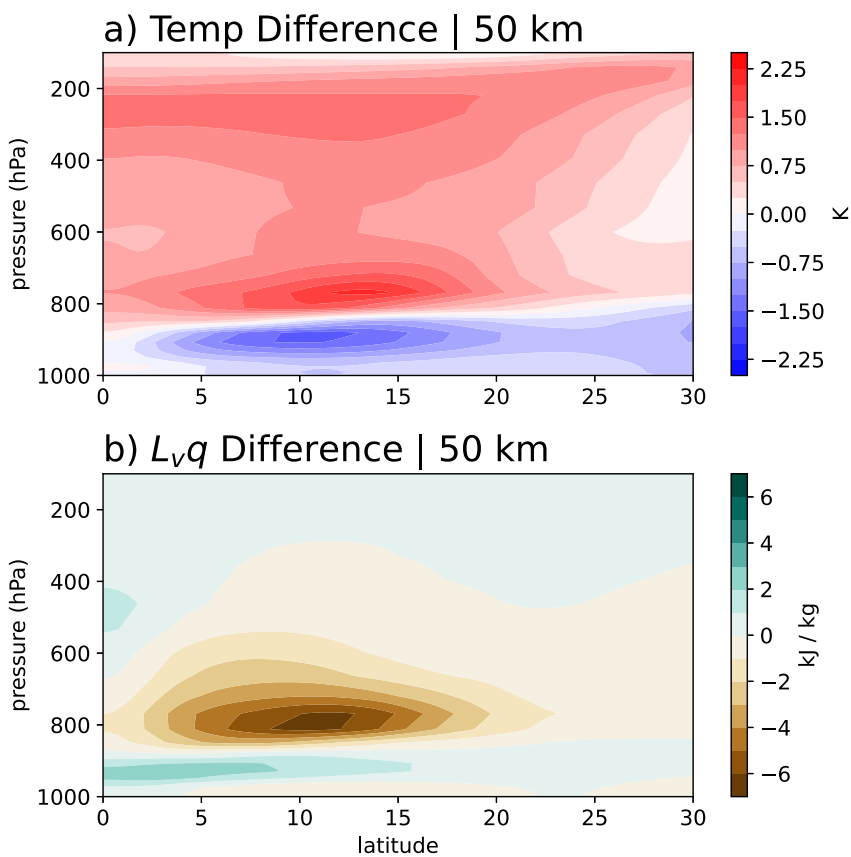

Figure 9. The difference (off minus on) between the climatological zonal mean (a) temperature and (b) latent energy in an AM4-MG2 at 50 km resolution.

dynamic term is negative, the circulation has shallowed. In contrast, poleward of about 4°, where the dynamic Δ_{MMC} change is positive, we expect the circulation to be more top-heavy. To investigate this further, in Figure 6b we plot the meridional wind profiles, normalized by v_L at the native vertical resolution.

Over the 6–10° latitude range, Figure 6b shows that 50 km_off simulates greater poleward mass flux than 50 km_on above 300 hPa and between 700 and 800 hPa but reduced poleward mass flux between 700 and 300 hPa. The reduced $-\frac{v_M}{v_L}$ over 6–10° mainly results from the change in poleward mass flux above 300 hPa. Over the 0–2° latitude range, where the dynamic component is negative, 50 km_off simulates poleward flow over a deeper layer from ∼800 hPa to ∼150 hPa, which increases $-\frac{v_M}{v_L}$ and thus reduces Δ_{MMC}.

In contrast with the dynamic component to the Δ_{MMC} change, the thermodynamic component is positive at all latitudes in the deep tropics (Figure 5b). Based on the Held (2001) scaling, the thermodynamic component to the Δ_{MMC} change reflects the ITCZ moistening at a greater rate than poleward latitudes in the tropics (Figures 5b and 9b). This is due to low-level moisture flux strengthening in the core of the ITCZ, consistent with strengthened equatorward flow and a moister boundary layer, causing the low-level MSE gradient to strengthen.

3.6. Discussion

Whether the model resolution is 50 km or 6 km, much of the ITCZ response to disabling parameterized convection can be attributed to disabling the shallow plume. So, why does the ITCZ response to disabling shallow convection differ so dramatically with resolution? This is because shallow convection impacts the climate system through multiple pathways, leading to a diversity of responses across different models and model configurations (e.g., Webb et al., 2015). In our case, a better understanding of these pathways can be gained by examining the components of the ITCZ response, δ_{AEI} and $\delta_{\Delta h}$.

As alluded to in Section 3.3, the resolution dependence of δ_{AEI} is owed in large part to the resolution dependence of the mean state GMS. This is because, for a given perturbation in energy flux F, the corresponding change in mass flux is given by $F\Delta h^{-1}$. Considering that the mean state value of Δh^{-1} is roughly halved when the resolution changes from 50 to 6 km (Figure 2b), so too does a mass flux response to any identical perturbation in AEI. This implies that the ITCZ simulated by the 6 km model is less sensitive to changes in AEI, including changes in low-cloud longwave radiative cooling.

The resolution dependence of $\delta_{\Delta h}$ is more complex as this quantity is determined largely by how the vertical structure of the MMC is changed by disabling parameterized convection. Specifically, why does disabling parameterized convection favor a top-heavy MMC at 6 km resolution, but not at 50 km resolution? In Figure 10, we hypothesize that subtle differences in the vertical profiles of diabatic heating in the subsidence region are responsible for changes in the MMC vertical structure (see also Figure S6 in Supporting Information S1). This hypothesis is consistent with previous work showing that diabatic heating in subsidence regions can affect the vertical structure of overturning circulations (e.g., Flaschner et al., 2018; Muller & Bony, 2015; Muller & Held, 2012).

As shown in Figures 10a–10c, when the convection scheme is enabled, latent heating produces a moderate low-level heating of ∼3 K/day near the ∼950 hPa level (solid blue), regardless of the model resolution, with much of this heating coming from the convective parameterization (dashed blue). In contrast, when the convection scheme is disabled, the low-level latent heating intensifies dramatically as grid-scale motion becomes the only means through which clouds can form. Despite the large increase in latent heating however, disabling parameterized convection has only a subtle impact on total diabatic heating due to a compensation from increased low-cloud longwave cooling. Nonetheless, we argue that these subtle differences in the total diabatic term may be enough to help shape the vertical structure of the MMC.

Of interest is a modest peak in total diabatic cooling within the 800–850 hPa layer that occurs in all models except 6 km_off (Figure 10). In all models except 6 km_off, this diabatic cooling peak implies peak subsidence within the 800–850 hPa layer (assuming a balance between diabatic cooling and adiabatic warming), and therefore a divergence of vertical pressure velocity within the overlying layer, ∼750–800 hPa. As the implied divergence of vertical pressure velocity in the ∼750–800 hPa layer would need to be balanced by a convergence of meridional wind, we argue that the existence of peak diabatic cooling the 800–850 hPa layer drives the shallow component to the MMC. Accordingly, our hypothesis is that the top-heavy MMC in 6 km_off is due to the absence of peak

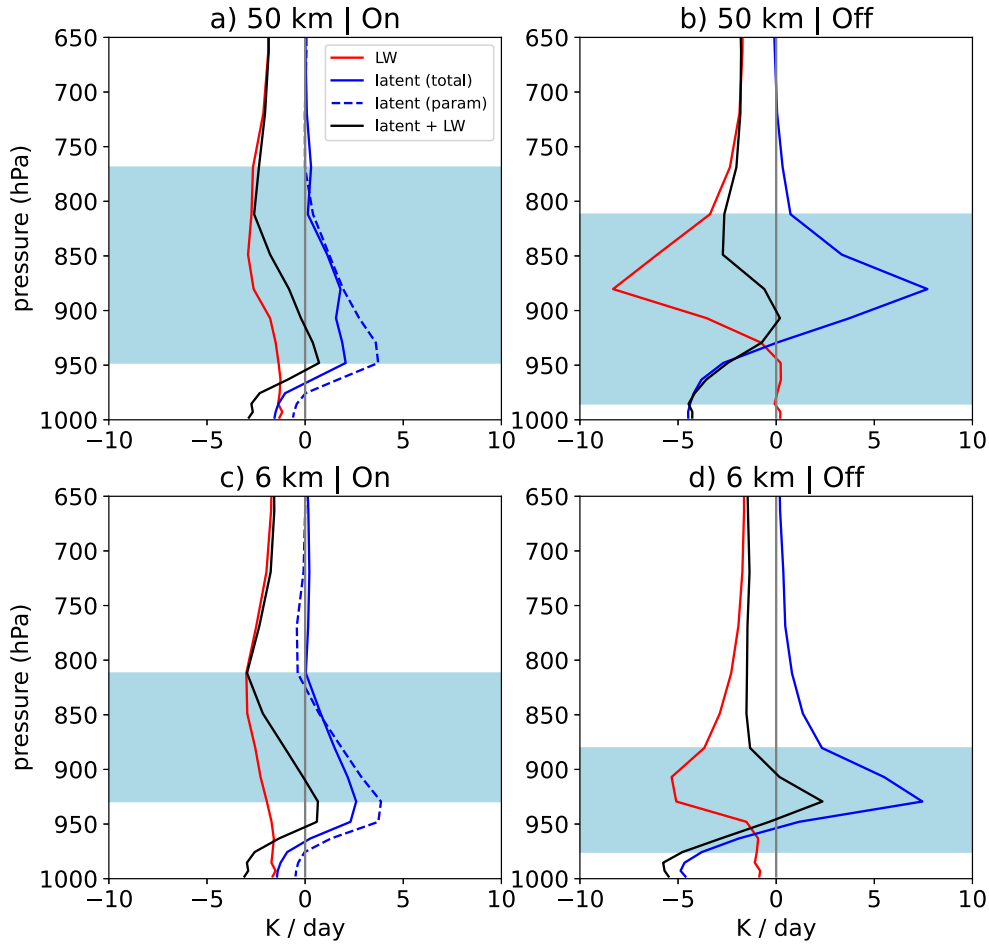

Figure 10. Vertical profiles of longwave radiative heating (red), total latent heating (convective plus large-scale; solid blue), and convective latent heating (dashed blue) averaged over the descending region (5°–20°) in (a) 50 km_on, (b) 50 km_off, (c) 6 km_on and (d) 6 km_off. The shading shows where cloud fraction exceeds 5%. The black line shows the sum of the longwave radiative heating rate with the latent heating rate.

cooling within the 800–850 hPa layer and, following this logic, the resolution dependence of the MMC vertical structure may partly stem from the vertical structure of longwave radiation and latent heating in the lower troposphere of the subsidence region.

4. Summary and Conclusions

As model resolutions continue to increase, it remains unclear how disabling the convection scheme will change the ITCZ and why, motivating our study of the physical processes controlling changes in the ITCZ when the convection scheme is deactivated at 50 and 6 km resolutions. We find that the ITCZ has a resolution dependent response to the convection scheme: at 50 km resolution, when the convection scheme is turned off, the ITCZ narrows and the P–E maximum nearly doubles. In strong contrast, at 6 km, when the convection scheme is turned off, the ITCZ widens and the P–E maximum nearly halves.

A consequence of turning the convection scheme off at 50 km is a buildup of low clouds in the subsidence region of the Hadley circulation. This is consistent with more low-level moisture and a stronger inversion at the boundary layer top when the convection scheme is deactivated. The stronger longwave cloud radiative cooling in the subsidence region requires a stronger overturning circulation to transport more energy poleward, which is the leading driver for the stronger moisture convergence and thus ITCZ. In addition, GMS decreases near the equator and increases off the equator, contributing to a narrowing of the ITCZ.

In contrast with the 50 km model, when the convection scheme is disabled at 6 km, the total GMS increases throughout the ITCZ, driving a decrease in P–E. This results from the fraction of poleward mass flux in the upper troposphere increasing at the expense of that in the middle troposphere. We suspect that the top-heavy overturning circulation is in response to disabling the parameterized shallow convection, since the deep convection is largely resolved at 6 km and the deep convection parameterization has a small impact at this resolution.

In idealized cloud resolving models and in more comprehensive GCMs, studies have shown that shallow overturning circulations are important for aggregating convection, as shallower overturning circulations are less efficient at exporting MSE (e.g., Flaschner et al., 2018; Muller & Bony, 2015; Muller & Held, 2012). Interestingly, these studies suggest that low-cloud radiative cooling, in otherwise clear-sky subsidence regions, can promote shallower overturning circulations. Here, we find that the excessive low clouds may not always lead to a stronger shallow circulation depending on the compensation between the radiative cooling and the condensational heating. Our results highlight the sensitivity of the shallow circulation to the detailed structure of the diabatic heating over the subsidence regions.

It is important to note that the results reported here are limited to one convection scheme and model setup. In a fixed SST framework, disabling parameterized convection (both deep and shallow) is likely to increase low clouds over a wide range of coarse resolutions (e.g., Hohenegger et al., 2020). However, with a coupled surface, such as a slab ocean, the cloud response could change significantly due to changes in the SST, which is particularly relevant for 50 km results shown here, where downwelling surface longwave fluxes changed significantly. Many studies have also revealed that changing the SST profile can impact the ITCZ width and intensity (e.g., Watt-Meyer and Frierson (2019); Neale & Hoskins, 2000; Watt-Meyer and Frierson (2019)), which highlights the need to investigate how these results change if the SST profile is changed. Furthermore, it is not clear how ocean feedbacks would factor in if the lower boundary was more realistic. For example, Ekman advection may play a role in setting the position of the ITCZ (e.g., Kang et al., 2018; Schneider, 2017; Schneider et al., 2014).

Interestingly, the 50 km results reported here corroborate several previous studies where disabling the convection scheme at resolutions coarser than storm resolving scales intensified the ITCZ (e.g., Frierson, 2007; Möbis & Stevens, 2012; Retsch et al., 2019). We find that the response at this coarse resolution is primarily tied to low cloud radiative cooling, offering a different physical interpretation for the ITCZ response. Since this could in part be related to the fact that both deep and shallow convection are handled by the same convection scheme, future work should investigate using different models. Nonetheless, that the response to disabling convection is opposite at 6 km resolution also implies that there is a resolution range for which disabling the convection scheme may not change the ITCZ. This raises a question that we defer to future work, that is, with disabled parameterized convection, what resolution is required for the meridional profile of P–E to converge?

While the results here are limited to one model setup and two horizontal resolutions, they may serve as a starting point for understanding the means through which the convection scheme changes the ITCZ, particularly as resolutions approach storm resolving scales where one may consider whether or not to implement parameterized convection.

Data Availability Statement

The model code, build and configuration files are provided by Robinson et al. (2022). Model output data used in this study is provided by Clark (2023).

Acknowledgments
We thank Nadir Jeevanjee, Zhihong Tan, Ming Zhao, David Paynter and Yi Ming for insightful conversations. This report was prepared by JPC, PL and SAH under award NA18OAR4320123 from the National Oceanic and Atmospheric Administration, U.S. Department of Commerce. The statements, findings, conclusions, and recommendations are those of the author(s) and do not necessarily reflect the views of the National Oceanic and Atmospheric Administration, or the U.S. Department of Commerce. SAH is also supported by NSF grant AGS-2123327. We acknowledge GFDL resources made available for this research.

References

Benedict, J. J., Medeiros, B., Clement, A. C., & Pendergrass, A. G. (2017). Sensitivities of the hydrologic cycle to model physics, grid resolution, and ocean type in the aquaplanet community atmosphere model. *Journal of Advances in Modeling Earth Systems*, *9*(2), 1307–1324. https://doi.org/10.1002/2016ms000891

Bischoff, T., & Schneider, T. (2014). Energetic constraints on the position of the intertropical convergence zone. *Journal of Climate*, *27*(13), 4937–4951. https://doi.org/10.1175/jcli-d-13-00650.1

Bischoff, T., & Schneider, T. (2016). The equatorial energy balance, ITCZ position, and double-ITCZ bifurcations. *Journal of Climate*, *29*(8), 2997–3013. https://doi.org/10.1175/jcli-d-15-0328.1

Bretherton, C. S., McCaa, J. R., & Grenier, H. (2004). A new parameterization for shallow cumulus convection and its application to marine subtropical cloud-topped boundary layers. Part I: Description and 1D results. *Monthly Weather Review*, *132*(4), 864–882. https://doi.org/10.1175/1520-0493(2004)132<0864:anpfsc>2.0.co;2

Broccoli, A. J., Dahl, K. A., & Stouffer, R. J. (2006). Response of the ITCZ to northern hemisphere cooling. *Geophysical Research Letters*, *33*(1). https://doi.org/10.1029/2005gl024546

Bryan, G. H., Wyngaard, J. C., & Fritsch, J. M. (2003). Resolution requirements for the simulation of deep moist convection. *Monthly Weather Review*, *131*(10), 2394–2416. https://doi.org/10.1175/1520-0493(2003)131<2394:rrftso>2.0.co;2

Byrne, M. P., Pendergrass, A. G., Rapp, A. D., & Wodzicki, K. R. (2018). Response of the intertropical convergence zone to climate change: Location, width, and strength. *Current Climate Change Reports*, *4*(4), 355–370. https://doi.org/10.1007/s40641-018-0110-5

Byrne, M. P., & Schneider, T. (2016a). Energetic constraints on the width of the intertropical convergence zone. *Journal of Climate*, *29*(13), 4709–4721. https://doi.org/10.1175/jcli-d-15-0767.1

Byrne, M. P., & Schneider, T. (2016b). Narrowing of the ITCZ in a warming climate: Physical mechanisms. *Geophysical Research Letters*, *43*(21), 11–350. https://doi.org/10.1002/2016gl070396

Chao, W. C., & Chen, B. (2004). Single and double ITCZ in an aqua-planet model with constant sea surface temperature and solar angle. *Climate Dynamics*, *22*(4), 447–459. https://doi.org/10.1007/s00382-003-0387-4

Clark, J. P. (2023). AM4 output data for Clark, Lin, Hill (2023) [Dataset]. *Zenodo*. https://doi.org/10.5281/zenodo.8244904

Colman, R. A., & McAvaney, B. J. (1997). A study of general circulation model climate feedbacks determined from perturbed sea surface temperature experiments. *The Journal of Geophysical Research: Atmospheres*, *102*(D16), 19383–19402. https://doi.org/10.1029/97jd00206

de Szoeke, S. P., Wang, Y., Xie, S. P., & Miyama, T. (2006). Effect of shallow cumulus convection on the eastern Pacific climate in a coupled model. *Geophysical Research Letters*, *33*(17). https://doi.org/10.1029/2006gl026715

Dixit, V., Geoffroy, O., & Sherwood, S. C. (2018). Control of ITCZ width by low-level radiative heating from upper-level clouds in aquaplanet simulations. *Geophysical Research Letters*, *45*(11), 5788–5797. https://doi.org/10.1029/2018gl078292

Fläschner, D., Mauritsen, T., Stevens, B., & Bony, S. (2018). The signature of shallow circulations, not cloud radiative effects, in the spatial distribution of tropical precipitation. *Journal of Climate*, *31*(23), 9489–9505. https://doi.org/10.1175/jcli-d-18-0230.1

Frierson, D. M. (2007). The dynamics of idealized convection schemes and their effect on the zonally averaged tropical circulation. *Journal of the Atmospheric Sciences*, *64*(6), 1959–1976. https://doi.org/10.1175/jas3935.1

Gettelman, A., & Morrison, H. (2015). Advanced two-moment bulk microphysics for global models. Part I: Off-line tests and comparison with other schemes. *Journal of Climate*, *28*(3), 1268–1287. https://doi.org/10.1175/jcli-d-14-00102.1

Guo, H., Ming, Y., Fan, S., Zhou, L., Harris, L., & Zhao, M. (2021). Two-Moment bulk cloud microphysics with prognostic precipitation in GFDL's atmosphere model AM4. 0: Configuration and performance. *Journal of Advances in Modeling Earth Systems*, *13*(6), e2020MS002453. https://doi.org/10.1029/2020ms002453

Harris, L., Chen, X., Zhou, L., & Chen, J. H. (2020). The nonhydrostatic solver of the GFDL finite-volume cubed-sphere dynamical core. https://doi.org/10.25923/9wdt-4895

Harrop, B. E., & Hartmann, D. L. (2016). The role of cloud radiative heating in determining the location of the ITCZ in aquaplanet simulations. *Journal of Climate*, *29*(8), 2741–2763. https://doi.org/10.1175/jcli-d-15-0521.1

Held, I. M. (2001). The partitioning of the poleward energy transport between the Tropical Ocean and atmosphere. *Journal of the Atmospheric Sciences*, *58*(8), 943–948. https://doi.org/10.1175/1520-0469(2001)058<0943:tpotpe>2.0.co;2

Hess, P. G., Battisti, D. S., & Rasch, P. J. (1993). Maintenance of the intertropical convergence zones and the large-scale tropical circulation on a water-covered earth. *Journal of the Atmospheric Sciences*, *50*(5), 691–713. https://doi.org/10.1175/1520-0469(1993)050<0691:moticz>2.0.co;2

Hill, S. A. (2019). Theories for past and future monsoon rainfall changes. *Current Climate Change Reports*, *5*(3), 160–171. https://doi.org/10.1007/s40641-019-00137-8

Hill, S. A., Ming, Y., & Held, I. M. (2015). Mechanisms of forced tropical meridional energy flux change. *Journal of Climate*, *28*(5), 1725–1742. https://doi.org/10.1175/jcli-d-14-00165.1

Hohenegger, C., Kornblueh, L., Klocke, D., Becker, T., Cioni, G., Engels, J. F., et al. (2020). Climate statistics in global simulations of the atmosphere, from 80 to 2.5 km grid spacing. *Journal of the Meteorological Society of Japan. Ser. II*, *98*(1), 73–91. https://doi.org/10.2151/jmsj.2020-005

Kang, S. M., Frierson, D. M., & Held, I. M. (2009). The tropical response to extratropical thermal forcing in an idealized GCM: The importance of radiative feedbacks and convective parameterization. *Journal of the Atmospheric Sciences*, *66*(9), 2812–2827. https://doi.org/10.1175/2009jas2924.1

Kang, S. M., Held, I. M., Frierson, D. M., & Zhao, M. (2008). The response of the ITCZ to extratropical thermal forcing: Idealized slab-ocean experiments with a GCM. *Journal of Climate*, *21*(14), 3521–3532. https://doi.org/10.1175/2007jcli2146.1

Kang, S. M., Shin, Y., & Xie, S. P. (2018). Extratropical forcing and tropical rainfall distribution: Energetics framework and ocean Ekman advection. *NPJ Climate and Atmospheric Science*, *1*(1), 1–10. https://doi.org/10.1038/s41612-017-0004-6

Landu, K., Leung, L. R., Hagos, S., Vinoj, V., Rauscher, S. A., Ringler, T., & Taylor, M. (2014). The dependence of ITCZ structure on model resolution and dynamical core in aquaplanet simulations. *Journal of Climate*, *27*(6), 2375–2385. https://doi.org/10.1175/jcli-d-13-00269.1

Lin, J. L. (2007). The double-ITCZ problem in IPCC AR4 coupled GCMs: Ocean–atmosphere feedback analysis. *Journal of Climate*, *20*(18), 4497–4525. https://doi.org/10.1175/jcli4272.1

Lin, P., Ming, Y., & Robinson, T. (2023). On the resolution sensitivity of equatorial precipitation in a GFDL global atmospheric model. *Journal of Advances in Modeling Earth Systems*, *15*(10), e2022MS003300. https://doi.org/10.1029/2022ms003300

Liu, Y., Guo, L., Wu, G., & Wang, Z. (2010). Sensitivity of ITCZ configuration to cumulus convective parameterizations on an aqua planet. *Climate Dynamics*, *34*(2), 223–240. https://doi.org/10.1007/s00382-009-0652-2

Marshall, J., Donohoe, A., Ferreira, D., & McGee, D. (2014). The ocean's role in setting the mean position of the Inter-Tropical Convergence Zone. *Climate Dynamics*, *42*(7–8), 1967–1979. https://doi.org/10.1007/s00382-013-1767-z

McCaa, J. R., & Bretherton, C. S. (2004). A new parameterization for shallow cumulus convection and its application to marine subtropical cloud-topped boundary layers. Part II: Regional simulations of marine boundary layer clouds. *Monthly Weather Review*, *132*(4), 883–896. https://doi.org/10.1175/1520-0493(2004)132<0883:anpfsc>2.0.co;2

Mishra, S. K., Srinivasan, J., & Nanjundiah, R. S. (2008). The impact of the time step on the intensity of ITCZ in an aquaplanet GCM. *Monthly Weather Review*, *136*(11), 4077–4091. https://doi.org/10.1175/2008mwr2478.1

Möbis, B., & Stevens, B. (2012). Factors controlling the position of the intertropical convergence zone on an aquaplanet. *Journal of Advances in Modeling Earth Systems*, *4*(4). https://doi.org/10.1029/2012ms000199

Muller, C., & Bony, S. (2015). What favors convective aggregation and why? *Geophysical Research Letters*, *42*(13), 5626–5634. https://doi.org/10.1002/2015gl064260

Muller, C. J., & Held, I. M. (2012). Detailed investigation of the self-aggregation of convection in cloud-resolving simulations. *Journal of the Atmospheric Sciences*, *69*(8), 2551–2565. https://doi.org/10.1175/jas-d-11-0257.1

Neale, R. B., & Hoskins, B. J. (2000). A standard test for AGCMs including their physical parametrizations: I: The proposal. *Atmospheric Science Letters*, *1*(2), 101–107. https://doi.org/10.1006/asle.2000.0019

Neelin, J. D., & Held, I. M. (1987). Modeling tropical convergence based on the moist static energy budget. *Monthly Weather Review*, *115*(1), 3–12. https://doi.org/10.1175/1520-0493(1987)115<0003:mtcbot>2.0.co;2

Neelin, J. D., & Yu, J. Y. (1994). Modes of tropical variability under convective adjustment and the Madden–Julian oscillation. Part I: Analytical theory. *Journal of the Atmospheric Sciences*, *51*(13), 1876–1894. https://doi.org/10.1175/1520-0469(1994)051<1876:motvuc>2.0.co;2

Nolan, D. S., Tulich, S. N., & Blanco, J. E. (2016). ITCZ structure as determined by parameterized versus explicit convection in aquachannel and aquapatch simulations. *Journal of Advances in Modeling Earth Systems*, *8*(1), 425–452. https://doi.org/10.1002/2015ms000560

Pauluis, O., & Garner, S. (2006). Sensitivity of radiative–convective equilibrium simulations to horizontal resolution. *Journal of the Atmospheric Sciences*, *63*(7), 1910–1923. https://doi.org/10.1175/jas3705.1

Popp, M., & Silvers, L. G. (2017). Double and single ITCZs with and without clouds. *Journal of Climate*, *30*(22), 9147–9166. https://doi.org/10.1175/jcli-d-17-0062.1

Raymond, D. J., Sessions, S. L., Sobel, A. H., & Fuchs, Ž. (2009). The mechanics of gross moist stability. *Journal of Advances in Modeling Earth Systems*, *1*(3). https://doi.org/10.3894/james.2009.1.9

Retsch, M. H., Hohenegger, C., & Stevens, B. (2017). Vertical resolution refinement in an aqua-planet and its effect on the ITCZ. *Journal of Advances in Modeling Earth Systems*, *9*(6), 2425–2436. https://doi.org/10.1002/2017ms001010

Retsch, M. H., Mauritsen, T., & Hohenegger, C. (2019). Climate change feedbacks in aquaplanet experiments with explicit and parametrized convection for horizontal resolutions of 2,525 up to 5 km. *Journal of Advances in Modeling Earth Systems*, *11*(7), 2070–2088. https://doi.org/10.1029/2019ms001677

Rios-Berrios, R., Bryan, G. H., Medeiros, B., Judt, F., & Wang, W. (2022). Differences in tropical rainfall in aquaplanet simulations with resolved or parameterized deep convection. *Journal of Advances in Modeling Earth Systems*, *14*(5), e2021MS002902. https://doi.org/10.1029/2021ms002902

Robinson, T., Radhakrishnan, A., & Underwood, S. (2022). NOAA-GFDL/AM4: Non-hydrostatic aquaplanet MG. *Zenodo*. [high-res_aquaplanet_2022]. https://doi.org/10.5281/zenodo.7476908

Schneider, T. (2017). Feedback of atmosphere-ocean coupling on shifts of the Intertropical Convergence Zone. *Geophysical Research Letters*, *44*(22), 11–644. https://doi.org/10.1002/2017gl075817

Schneider, T., Bischoff, T., & Haug, G. H. (2014). Migrations and dynamics of the intertropical convergence zone. *Nature*, *513*(7516), 45–53. https://doi.org/10.1038/nature13636

Skamarock, W. C., Klemp, J. B., Duda, M. G., Fowler, L. D., Park, S. H., & Ringler, T. D. (2012). A multiscale nonhydrostatic atmospheric model using centroidal Voronoi tesselations and C-grid staggering. *Monthly Weather Review*, *140*(9), 3090–3105. https://doi.org/10.1175/mwr-d-11-00215.1

Skamarock, W. C., Klemp, J. B., Dudhia, J., Gill, D. O., Barker, D. M., Duda, M. G., et al. (2008). *A description of the advanced research WRF version 3* (p. 113). NCAR Technical Note 475 + STR.

Song, X., & Zhang, G. J. (2018). The roles of convection parameterization in the formation of double ITCZ syndrome in the NCAR CESM: I. Atmospheric processes. *Journal of Advances in Modeling Earth Systems*, *10*(3), 842–866. https://doi.org/10.1002/2017ms001191

Stevens, B., Satoh, M., Auger, L., Biercamp, J., Bretherton, C. S., Chen, X., et al. (2019). Dyamond: The dynamics of the Atmospheric general circulation modeled on non-hydrostatic domains. *Progress in Earth and Planetary Science*, *6*(1), 1–17. https://doi.org/10.1186/s40645-019-0304-z

Tian, B., & Dong, X. (2020). The double-ITCZ bias in CMIP3, CMIP5, and CMIP6 models based on annual mean precipitation. *Geophysical Research Letters*, *47*(8), e2020GL087232. https://doi.org/10.1029/2020gl087232

Tiedtke, M. (1993). Representation of clouds in large-scale models. *Monthly Weather Review*, *121*(11), 3040–3061. https://doi.org/10.1175/1520-0493(1993)121<3040:rocils>2.0.co;2

Voigt, A., Stevens, B., Bader, J., & Mauritsen, T. (2014). Compensation of hemispheric albedo asymmetries by shifts of the ITCZ and tropical clouds. *Journal of Climate*, *27*(3), 1029–1045. https://doi.org/10.1175/jcli-d-13-00205.1

von Salzen, K., McFarlane, N. A., & Lazare, M. (2005). The role of shallow convection in the water and energy cycles of the atmosphere. *Climate Dynamics*, *25*(7–8), 671–688. https://doi.org/10.1007/s00382-005-0051-2

Watanabe, M., Kamae, Y., Shiogama, H., DeAngelis, A. M., & Suzuki, K. (2018). Low clouds link equilibrium climate sensitivity to hydrological sensitivity. *Nature Climate Change*, *8*(10), 901–906. https://doi.org/10.1038/s41558-018-0272-0

Watt-Meyer, O., & Frierson, D. M. (2019). ITCZ width controls on Hadley cell extent and eddy-driven jet position and their response to warming. *Journal of Climate*, *32*(4), 1151–1166. https://doi.org/10.1175/jcli-d-18-0434.1

Webb, M. J., Lock, A. P., Bretherton, C. S., Bony, S., Cole, J. N., Idelkadi, A., et al. (2015). The impact of parametrized convection on cloud feedback. *Philosophical Transactions of the Royal Society A: Mathematical, Physical & Engineering Sciences*, *373*(2054), 20140414. https://doi.org/10.1098/rsta.2014.0414

Weisman, M. L., Skamarock, W. C., & Klemp, J. B. (1997). The resolution dependence of explicitly modeled convective systems. *Monthly Weather Review*, *125*(4), 527–548. https://doi.org/10.1175/1520-0493(1997)125<0527:trdoem>2.0.co;2

Zhao, M., Golaz, J. C., Held, I. M., Guo, H., Balaji, V., Benson, R., et al. (2018a). The GFDL global atmosphere and land model AM4. 0/LM4. 0: 1. Simulation characteristics with prescribed SSTs. *Journal of Advances in Modeling Earth Systems*, *10*(3), 691–734. https://doi.org/10.1002/2017ms001208

Zhao, M., Golaz, J. C., Held, I. M., Guo, H., Balaji, V., Benson, R., et al. (2018b). The GFDL global atmosphere and land model AM4. 0/LM4. 0: 2. Model description, sensitivity studies, and tuning strategies. *Journal of Advances in Modeling Earth Systems*, *10*(3), 735–769. https://doi.org/10.1002/2017ms001209